# Double-pulse Laser Micro Sintering of Iron Powder in Multiple Overlapping Tracks: Experimental Study and Material Characterizations

Weidong Liu<sup>1</sup>, Benxin Wu<sup>1,\*</sup>, Runzi Cui<sup>2</sup>, Heng Wang<sup>2</sup>, Shunyu Liu<sup>3</sup>, Mohammadreza Asherloo<sup>2</sup>, Hanyu Song<sup>1</sup>

<sup>1</sup>School of Mechanical Engineering, Purdue University, West Lafayette IN, USA <sup>2</sup>Department of Mechanical, Materials and Aerospace Engineering, Illinois Institute of Technology, Chicago IL, USA

<sup>3</sup>Department of Automotive Engineering, Clemson University, Greenville, SC, USA

**Abstract:** Laser micro sintering (LMS) can be defined as a process producing micro features via laser-induced coalition of particles. In LMS, using short-pulse lasers and small particle sizes (a few µm or less) have potential advantages such as small theoretically achievable feature sizes. However, in this case it is often more challenging to obtain a highly densified material than conventional laser sintering. To help address this challenge, the corresponding author previously proposed a novel patented process named "double-pulse laser micro sintering" (DP-LMS), which typically utilizes "sintering laser pulses" to melt the powder and "pressing laser pulses" to induce in-situ transient high pressures on the powder surface to enhance densification. In this paper, DP-LMS of an iron powder layer with laser spot scanning multiple overlapping tracks has been studied, with sintered samples characterized via SEM, XRD, EDS and nanoindentation. The powder has a small original particle size of ~1.98 µm. Under the conditions studied, the surface porosity (surface pore area percentage) of material sintered by DP-LMS is ~3.4%, much lower than ~19.0%, the surface porosity of laser-sintered material without using DP-LMS. The material sintered with DP-LMS appears to have roughly equiaxed grains with typical sizes of ~1 to ~3 µm in the observed cross section region, and the small grain sizes should be related to the high cooling rate in re-solidification. The nanoindentation measurements show a high nanohardness of ~7.0 GPa for the material sintered with DP-LMS, which should be related to the small grain size and/or the existence of martensite. It has been found that to obtain a good DP-LMS result, an overlong melt pool lifetime induced by each laser pulse group should be avoided.

Keywords: additive manufacturing; laser micro sintering; pulsed laser sintering

### 1. Introduction

As common additive manufacturing technologies, selective laser melting and sintering can rapidly produce parts with good flexibility in material compositions and part geometries [1-5]. The part production is through layer-by-layer laser beam irradiation of a powder bed following controlled trajectories, causing coalition of powder particles in selected regions into more

<sup>\*</sup>Corresponding author: Benxin Wu, Professor, School of Mechanical Engineering, Purdue University, 585 Purdue Mall, West Lafayette, IN 47907, USA, email: <a href="www.wu65@purdue.edu">ww65@purdue.edu</a>

continuous features, typically via partial or complete melting of the particles [1]. In this paper, both the partial and full-melting situations will be called "laser sintering" for simplicity.

Although lasers in the continuous-wave mode are frequently utilized in **conventional laser sintering** [6-8], short-pulse lasers, such as lasers with nanosecond-scale pulse durations, may offer potential advantages, such as high spatial resolutions [9], high achievable transient laser intensities (which may be desirable for sintering high-melting-point materials) and/or a better adjustability of the target temperature history [10]. The potentially high spatial resolutions by short-pulsed lasers are particularly desirable when laser sintering is employed to make microscale geometrical features, in which case laser sintering can be named as "laser micro sintering" (LMS) [11-17]. In LMS, part features are produced by laser-induced coalition of multiple powder particles. Hence, smaller particles typically imply smaller theoretically achievable minimum feature sizes and higher spatial resolutions. Thus, in LMS, very small particle sizes of around a few  $\mu$ m (< ~10  $\mu$ m) or less are often used [11, 15], which are much smaller than the typical particle sizes of tens of  $\mu$ m or more in **conventional laser sintering** [15, 18-20].

Although using short-pulsed lasers and small metal particle sizes of a few µm or less have the aforementioned potential advantages in LMS, it is often more challenging to achieve high-densification and low-porosity material via short-pulsed laser sintering of the small particles than conventional laser sintering [15]. The small particles have large surface-to-volume ratios, and the inter-particle surface force may become significant relative to gravity [11]. The particles may often tend to agglomerate [11] and the sintering process may often be prone to balling and/or unthorough filling of inter-particle voids [11, 15, 17].

The corresponding author previously put forward a novel patented process named "double-pulse laser micro sintering" (abbreviated as: DP-LMS) [21] to enhance sintered

material densification and reduce balling and porosity. DP-LMS employs laser pulse groups comprising two kinds of laser pulses: the so-called "sintering pulses" and "pressing pulses". Typically, each sintering pulse is relatively long but has a low power density, intended to melt and coalesce powder particles. In each pulse group, after a certain number of sintering pulses are fired, one (or more) pressing laser pulse is sent at a controlled moment, at which the sintering pulses-induced molten material has not fully solidified. The pressing laser pulse is short but has a high power density. It can vaporize a very thin layer of the powder material, inducing a plasma plume and thus high pressures onto the molten material surface. The high pressures can potentially drive the flow of the molten material, enhance densification and continuity and/or reduce balling of the material upon solidification. Experimental studies on DP-LMS have been reported in the authors' previous papers [17, 22], showing that under the conditions investigated DP-LMS is able to result in much better densification and/or much less significant balling than laser sintering employing only the sintering or pressing pulses.

However, the authors' previous papers on DP-LMS [17, 22] only reported studies of very basic situations. In Ref. [22], multiple adjacent powder surface spots were sintered, and laser beams stayed stationary during the sintering of each spot, while Ref. [17] reported a study on single-track sintering (i.e., the laser beams scanned a single, non-overlapping track in each sintering). The sintered material's grain microstructures and mechanical properties (such as hardness) were not characterized in Refs. [17, 22]. To further advance the understanding of the relatively new DP-LMS process, in this paper DP-LMS of a powder layer with laser beams scanning multiple and overlapping tracks has been studied experimentally using nanosecond laser pulses and iron powder with a small original median particle diameter of ~1.98 μm. The top surface and cross sections of sintered material are observed using a scanning electron microscope (SEM).

The pore area percentage on the top surface has been obtained from SEM images via ImageJ [23] and compared with that for laser sintering employing only the "sintering pulses" (the latter will be called single-pulse laser micro sintering (SP-LMS) in this paper). The sintered material is characterized by X-ray diffraction (XRD) and energy-dispersive X-ray spectroscopy (EDS). The sintered material is chemically etched and observed by SEM for grain sizes and shapes. The material nanohardness has been measured via nanoindentation. Please note that this paper does NOT aim to investigate the spatial resolution achievable by DP-LMS. Thus, in this paper relatively big laser spots are utilized and powder bed surface regions on the ~mm scale are sintered to facilitate some material characterizations. But please note that with the small particle size, small micro features can be potentially produced with small laser spots.

DP-LMS itself does not require high-pressure compaction of powder particles prior to the sintering of each layer (the pre-sintering compaction may benefit the sintered material densification in LMS [15], but may also increase the manufacturing time). Meanwhile, DP-LMS does not prohibit the pre-sintering powder compaction, which can still be performed if it benefits the sintering result.

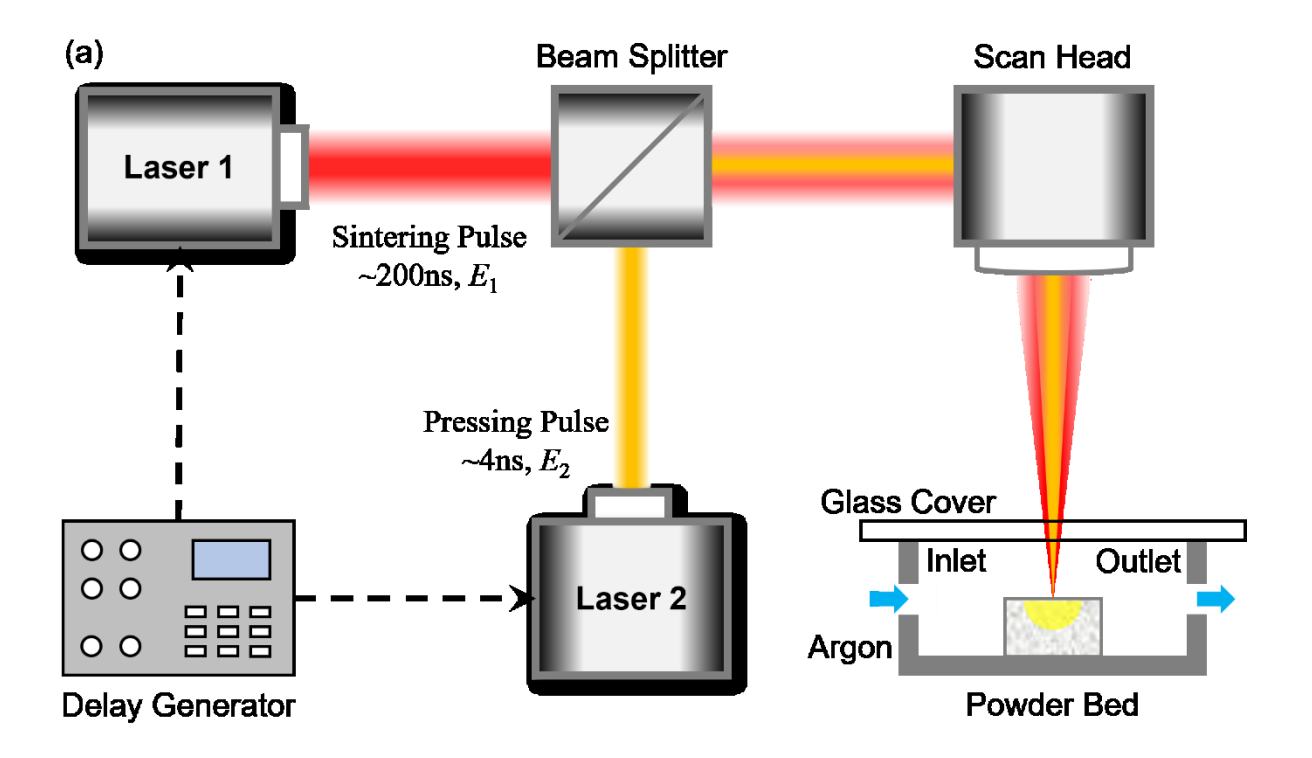
It should be noted that selective laser melting (SLM) of iron powders was reported in the literature, e.g., in Ref. [24]. However, Ref.[24] studied the SLM process based on a CW laser beam, not the unique DP-LMS process studied in this paper. Ref.[24] utilized an average powder particle size of  $\sim$ 27  $\mu$ m, much larger than the original median particle size in this paper ( $\sim$ 1.98  $\mu$ m). Thus, this work is very different from that in [24].

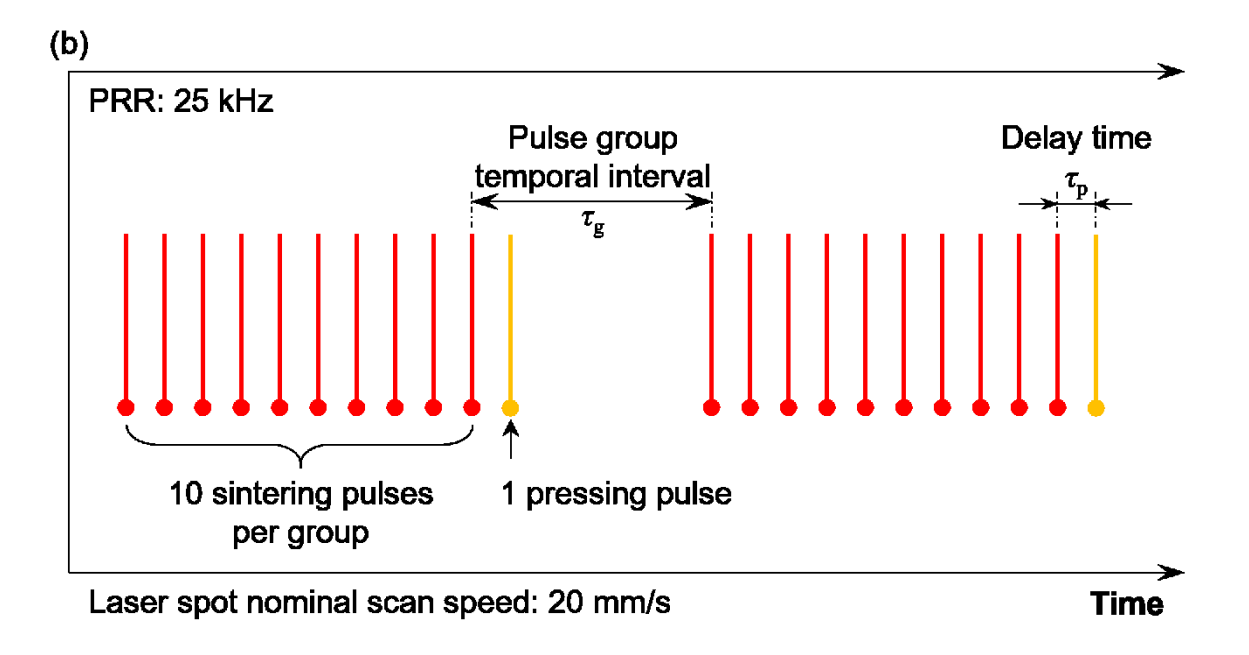
### 2. Experiment and Characterization

Figure 1a shows the major components of the DP-LMS system used in this experimental work. Laser 1 (SPI, G3.0) provides ~1064-nm "sintering pulses" with each pulse having a full duration equal to  $\sim 200$  ns and an average pulse energy equal to  $\sim 0.048$  mJ ( $E_1$ ). Laser 2 (Bright Solutions, Onda) provides ~1064-nm "pressing pulses" with each pulse having a full-width-athalf-maximum (FWHM) duration equal to ~4 ns and an average pulse energy equal to ~0.124 mJ  $(E_2)$ . The pulse energies  $E_1$  and  $E_2$  refer to those coming to the powder bed surface. The laser beam propagation paths of the two kinds of laser pulses are initially different, and then combined by the beam splitter in Fig.1 into approximately the same path. The two beams were aligned to be approximately coaxial after the beam splitter. Then they propagate into a scan head (Scanlab, Hurryscan 14), housing two mirrors controlling the laser spot scanning trajectory on the target surface, as well as a lens with a focal length equal to 100 mm. The sintering and pressing laser pulses have corresponding spot diameters of ~150 μm and ~110 μm, respectively, on the powder bed surface. The diameters were approximately estimated using the knife-edge method assuming approximately a Gaussian intensity profile for both laser beams. During laser scanning, the "pressing pulse" laser spot largely overlaps with the "sintering pulse" laser spot region on the powder bed surface, although the two laser spots may not be perfectly concentric. The powder bed surface is placed in a chamber with a transparent glass top cover. Prior to sintering, argon flows into the chamber for some time to displace air through the outlet of the chamber. During the sintering experiments, argon continues flowing. The average velocity of argon flow in the direction parallel to the powder bed surface is roughly estimated to be less than ~0.1 m/s, and thus the related cooling effect on the molten material is expected to be insignificant.

Figure 1b shows the typical sequence of laser pulses during the DP-LMS process studied in the work, achieved via the digital delay generator. In each pulse group, 10 sintering laser pulses

are shot with a temporal interval of 40  $\mu$ s between adjacent pulses, equivalent to a 25 kHz pulse repetition rate (PRR). Then, one pressing pulse is shot at a delay time ( $\tau_p$ ) equal to ~125  $\mu$ s after the 10<sup>th</sup> sintering laser pulse. After the current laser pulse group is finished, the next group begins at a temporal interval ( $\tau_g$ ) of ~640  $\mu$ s, which is the time interval from the last sintering pulse in the current pulse group to the first sintering pulse in the next pulse group.





**Figure 1**. Schematic diagrams showing: (a) the major components of the double-pulse laser micro sintering (DP-LMS) system used in the experiments; (b) the sequence of laser pulses in time during the DP-LMS process, where the line height does *not* represent the power of each pulse ( $E_1$  denotes the "sintering pulse" energy,  $E_2$  the "pressing pulse" energy, and  $\tau_p$  the "pressing pulse" delay time. Schematics in this paper do not necessarily comprise all components or present the exact actual details. The DP-LMS setup and the laser pulse sequence are similar to (but not exactly the same as) those shown in Fig.1 of the authors' prior paper Ref.[17]).

In this paper, the sintering of a powder-bed surface layer with laser beams scanning multiple overlapping tracks was conducted. Figure 2 shows the schematic for the laser spot scanning trajectory on the powder bed surface with a nominal scan speed of 20 mm/s. The scanning is bidirectional, where the directions of two adjacent tracks are opposite with a nominal hatch distance of  $50 \, \mu m$ . The nominal dimensions of the sintered regions on the powder bed surface are typically  $\sim 4.0 \, mm$  and  $\sim 1.5 \, mm$ . The aforementioned "nominal" speed and dimensions are the values used in the control parameters for the laser scan head in the sintering experiments.

In Figure 2, the scanning trajectory for DP-LMS was selected to be a bidirectional scanning trajectory mainly along the  $\pm Y$  direction with a nominal hatch distance of 50  $\mu$ m. It was found that

a unidirectional scanning or bidirectional scanning mainly along the  $\pm X$  direction led to much more significant thermal deformations of the sintered layer. Besides, under the given condition, a hatch distance of around ~50  $\mu$ m gave the lowest top surface porosity of the sintered layer compared with other hatch distances. Thus, the scanning trajectory as shown in Fig.2 was selected in this study.

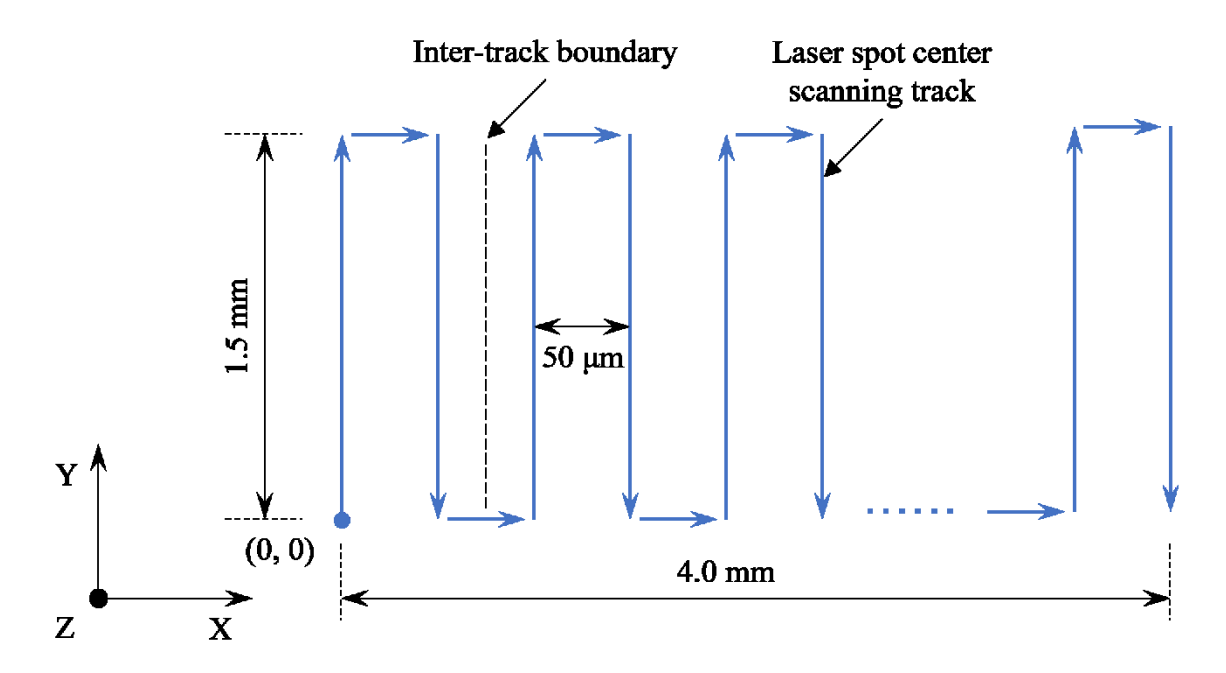


**Figure 2.** Schematic diagram of the laser spot scanning trajectory on the surface of the powder bed during DP-LMS for each iron layer sintered (the dashed line shows the "inter-track boundary", which is defined as the line in the middle of two adjacent laser scanning tracks).

The powder used in this work is the iron powder from Alfa Aesar (Product No.: 40337). Table 1 and 2 show the powder elemental composition and particle size distribution, respectively, which are based on the product Certificate of Analysis from Alfa Aesar [25] (in this paper the sintered material layer will be called an "iron layer" because iron is the dominant elemental component). The powder particles have an original median diameter of ~1.98 µm according to Ref. [25]. Before the sintering experiment, the iron powder was first put into ~95% ethanol and ultrasonically dispersed for a few minutes to decrease the possible agglomeration of the powder

particles. The supernatant was removed after the ultrasonic treatment was completed. Then the powder was manually stirred evenly with the residual ethanol using a micro spoon before it was distributed into the powder bed by a doctor blade. The iron powder in the bed got naturally dried in the air, after which the sintering experiments were carried out. The total powder thickness in the bed is  $\sim 200 \, \mu m$ , but the sintered layer is much thinner as shown later. According to the measured apparent volume and actual weight of the material in the powder bed, the pre-sintering density of the powder is estimated to be  $\sim 50\%$  of the corresponding bulk density of the material [25]. This value is obviously lower than the powder bed densities typically in the range of  $\sim 55$  to  $\sim 60\%$  reported in Refs. [18-20] for conventional laser sintering using larger powder particles with median diameters of tens of  $\mu m$  or more.

After the sintering process, the sintered iron layer was collected out of the powder bed, and then ultrasonically cleaned in water in an ultrasonic cleaner for a few seconds in order to remove particles attached to the bottom of the sintered iron layer. To prepare samples for SEM imaging of sample cross sections, nanoindentation test and chemical etching (for subsequent grain observation by SEM), sintered samples were mounted in epoxy resin, and their cross sections were ground on 180, 320, 600, 1200 and 2000-grit sandpapers sequentially, and then polished using 3 µm and 1 µm diamond suspensions sequentially. The samples intended for grain observation and indentation test went through a further polishing step utilizing a suspension of 0.05 µm colloidal silica. After this, the mounted samples were put into an ultrasonic cleaner to remove residual polishing suspension (if any) from the sample surfaces. The cross section of the sample for grain observation was etched with 2% nital (i.e., 98% ethanol + 2% nitric acid in terms of volume percentage) for around 12-15 seconds to reveal the grain microstructure for subsequent observation using SEM. SEM images were also taken for the un-polished top surface of some sintered samples.

Nanoindentation tests were carried out using the Keysight G200 Nanoindenter with the continuous stiffness measurement method [26] to obtain the nanohardness of the XZ cross section of some samples produced by the DP-LMS process. The maximum penetration depth of the tip is 300 nm. The hardness value given in this paper for each individual nanoindentation measurement is the average hardness for the tip penetration depth range of around 100 nm - 200nm.

In addition, X-ray diffraction (XRD) measurements were performed on both original iron powder and sintered iron samples using the Copper  $K_{\alpha}$  radiation in the measurements. The XRD measurement results provide useful information for phase identification in the material.

#### 3. Results and Discussions

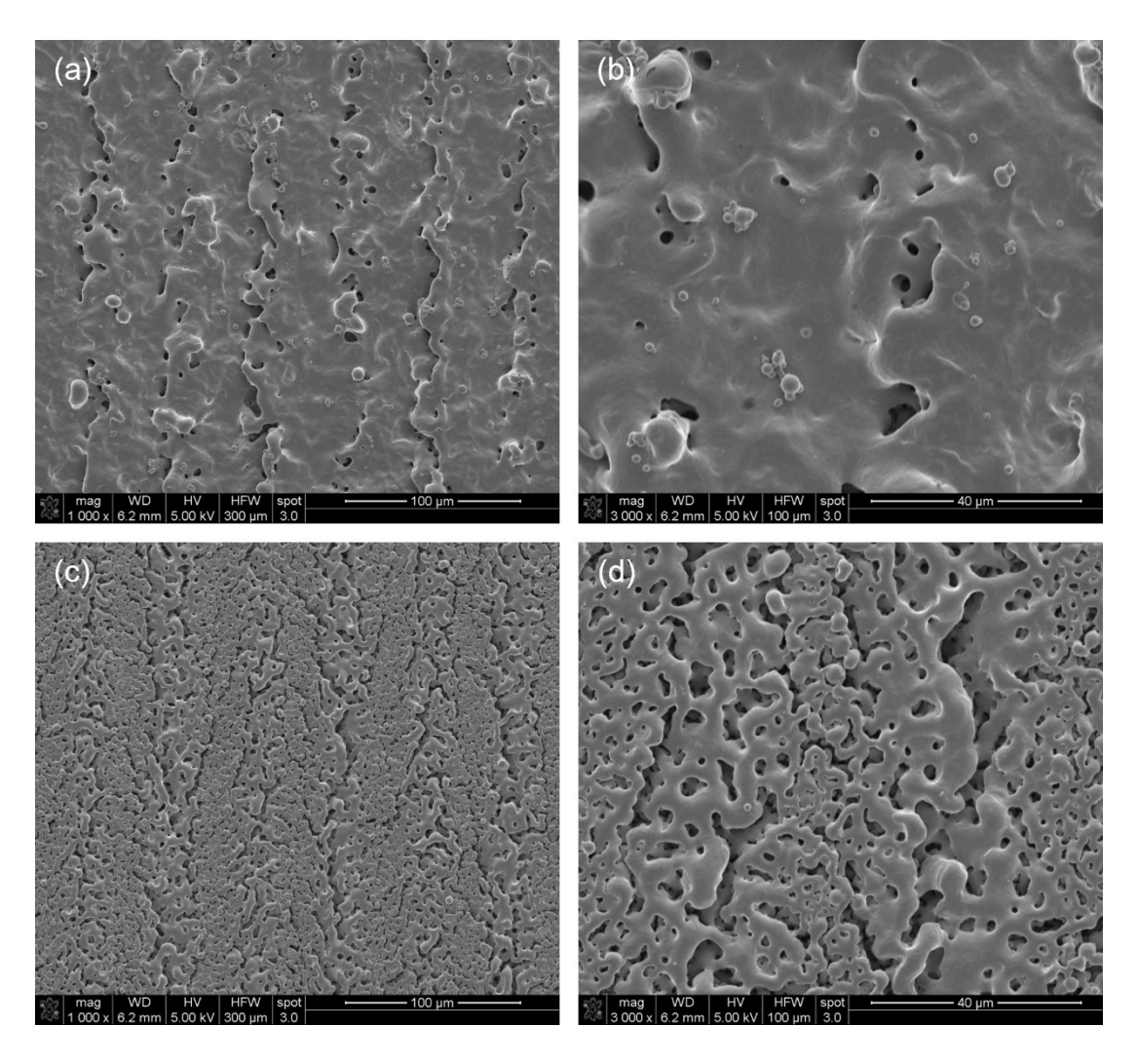
### 3.1 Morphology and Surface Porosity of Material Sintered by DP-LMS

Figure 3 gives the SEM images of the top surface of a sample sintered with DP-LMS (the top row) as well as the images of the top surface of a sample sintered using only the sintering pulses (denoted as "SP-LMS" in this paper). The images in Fig. 3b and 3d have a higher magnification than that in Fig. 3a and 3c. The SEM images demonstrate that the material sintered with DP-LMS looks much more densified and much less porous than the material sintered with SP-LMS.

Figure 3c and 3d show that if only the sintering pulses are used, the sintered material is not very continuous or densified; instead, highly porous network-like structures are formed. Laser-induced molten metal does not flow sufficiently to thoroughly fill inter-particle voids. The effects of the viscosity and/or surface tension of the molten metal likely play a role in hindering the thorough filling of voids via the molten metal flow [27].

On the other hand, Figure 3a and 3b show that the material sintered with DP-LMS appears reasonably continuous and densified, with some pores mainly located around inter-track boundaries. The porosity in Fig.3a and 3b appears much lower than that in Fig.3c and 3d. As already discussed in the authors' previous papers [17, 22], in DP-LMS typically the high-intensity pressing laser pulse can vaporize a very thin layer of material from the powder bed and generate a plasma plume above its surface. As a result, high transient pressures are induced onto the surface of the molten metal in the powder bed and promote the molten metal flow to better fill inter-particle voids to eventually achieve a more densified and less porous sintered material structure [11, 17, 22]. Figure 4 shows schematics demonstrating the aforementioned expected mechanisms for the different surface morphologies observed in Fig.3 for the material sintered with DP-LMS and SP-LMS.

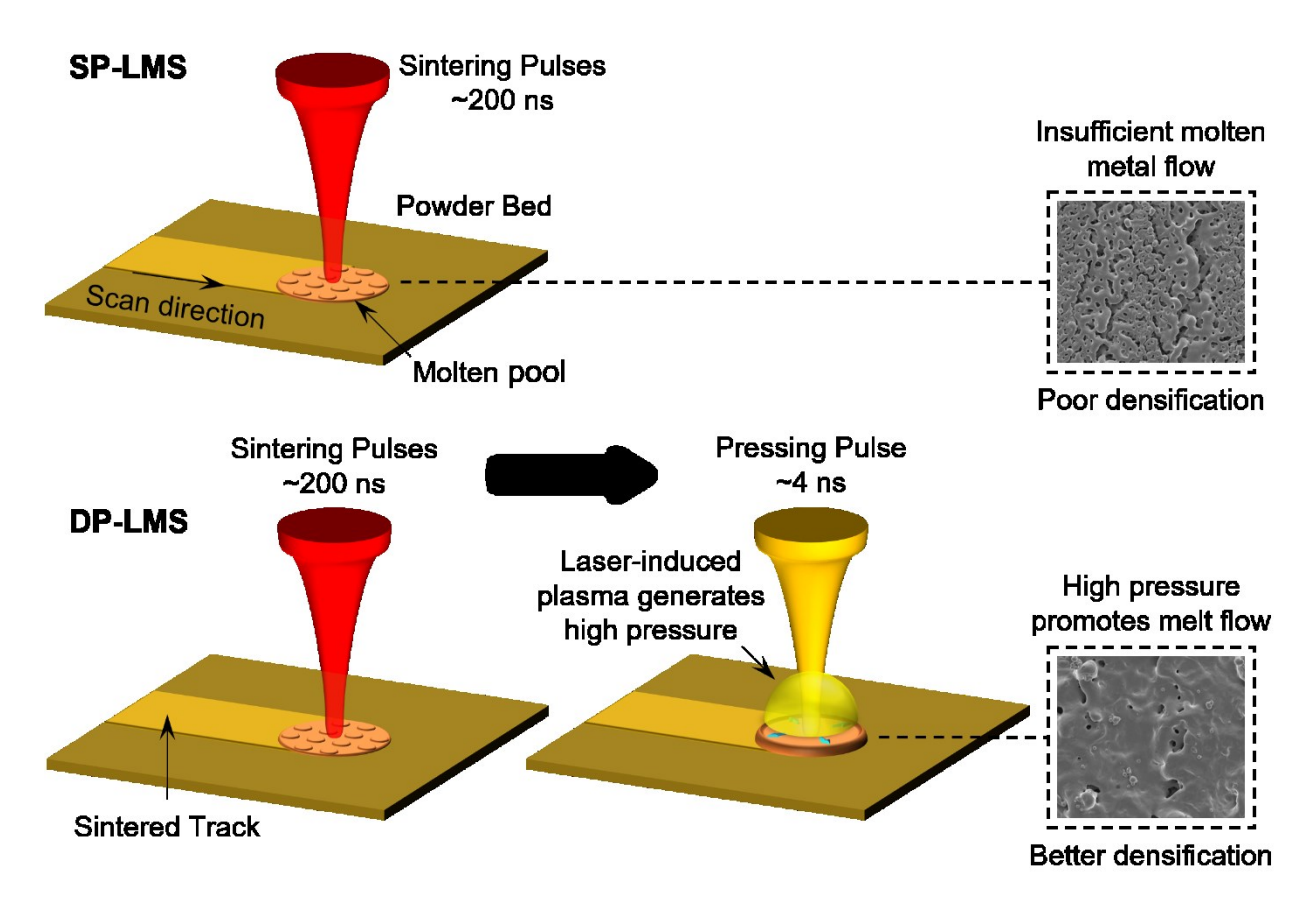
In DP-LMS, changing the relative position of the pressing pulse and sintering pulse laser spots will affect the relative impact position of the pressure induced by the pressing laser pulse. A small spot center distance is acceptable as long as the pressure can still effectively impact the region melted by the sintering pulse(s). But if the distance is too large and the melted region cannot be effectively impacted by the pressure, then the sintering result is expected to become obviously worse.



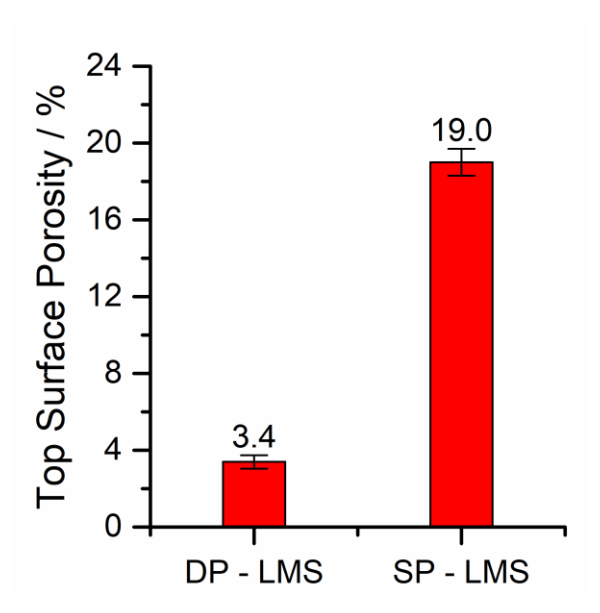
**Figure 3.** SEM images (for the XY plane view) of surface regions of material sintered with: (a)(b) DP-LMS, and (c)(d) LMS utilizing only the sintering pulses (denoted as SP-LMS) (see Fig.2 for the setup of the XYZ coordinate system).

Figure 5 shows the percentage of the pore area relative to the sintered material surface area (called "surface porosity" next for simplicity) in the imaged regions of samples sintered with DP-LMS versus the surface porosity with SP-LMS. Each surface porosity given in Fig. 5 is an average value from two samples sintered using the corresponding method (DP-LMS or SP-LMS). For each sample the surface porosity estimation is based on five SEM images taken at five different top surface regions roughly along the line of  $Y = \sim 0.75$  mm (see Figure 2 for the coordinate axis definition). Each imaged region has a size of  $\sim 300 \ \mu m \times \sim 260 \ \mu m$ . For each image, the pore area

percentage is obtained using ImageJ [23]. It can be seen that the surface porosity of the DP-LMS samples is ~3.4%, much lower than the surface porosity of the SP-LMS samples, which is ~19.0 %. This has quantitatively demonstrated the effectiveness of DP-LMS in improving densification and reducing porosity of sintered material as compared with the SP-LMS process.



**Figure 4.** Schematics of the expected fundamental mechanisms for the different surface morphologies of material sintered with SP-LMS and DP-LMS.



**Figure 5.** The top surface porosities of iron layers sintered with DP-LMS and SP-LMS (the "surface porosity" is defined as the pore area percentage in the measured surface regions).

Figure 6 shows SEM images for the XZ cross section of a sample sintered with DP-LMS (the top row) and a sample sintered with SP-LMS (the bottom row) (see Fig. 2 for the XYZ coordinate system definition). Figure 6b and 6d show further magnified portions of the regions in Figure 6a and 6c, respectively. Figure 7 shows the SEM images for the YZ cross section of a sample sintered with DP-LMS (the top row) and a sample with SP-LMS (the bottom row). Figure 7b and 7d show further magnified portions of the regions in Figure 7a and 7c, respectively.

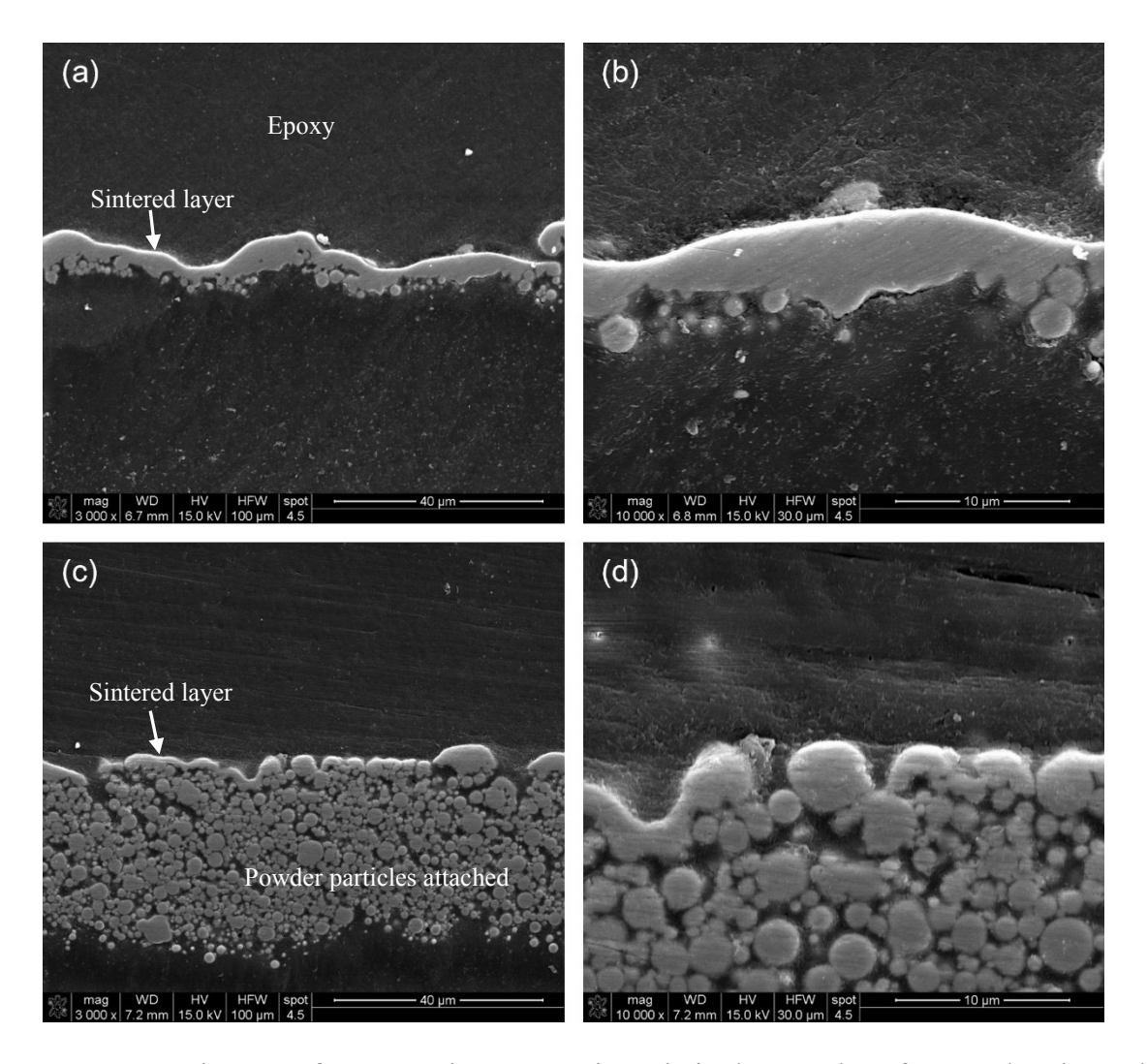


**Figure 6.** SEM images of cross sections approximately in the XZ plane for samples sintered with: (a)(b) DP-LMS, (c)(d) SP-LMS (see Fig.2 for the setup of the XYZ coordinate system).

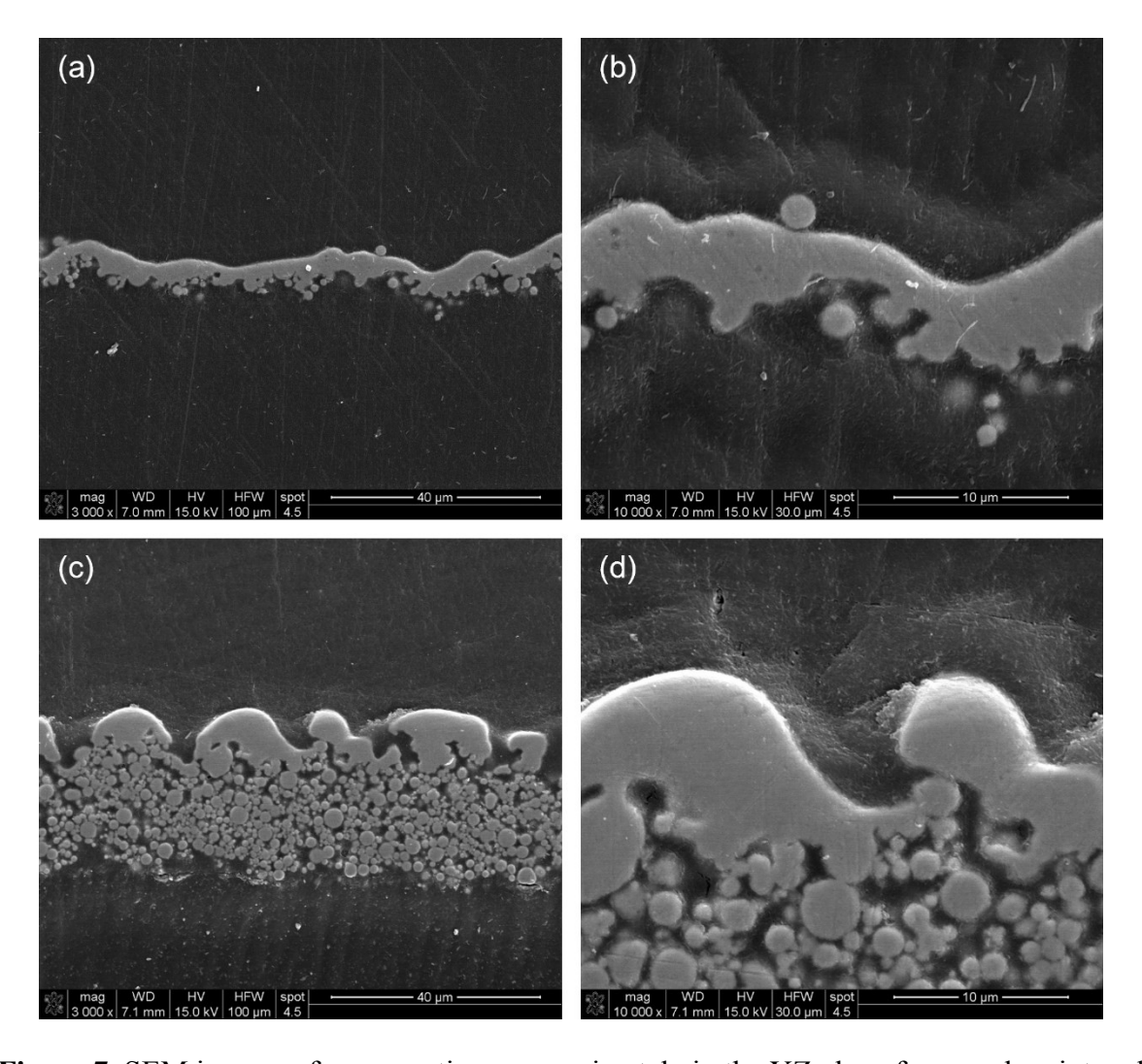


**Figure 7.** SEM images of cross sections approximately in the YZ plane for samples sintered with: (a)(b) DP-LMS, and (c)(d) SP-LMS (see Fig. 2 for the setup of the XYZ coordinate system. For (a)(b), the given YZ cross section is near the center of a Y-direction laser spot scanning trajectory).

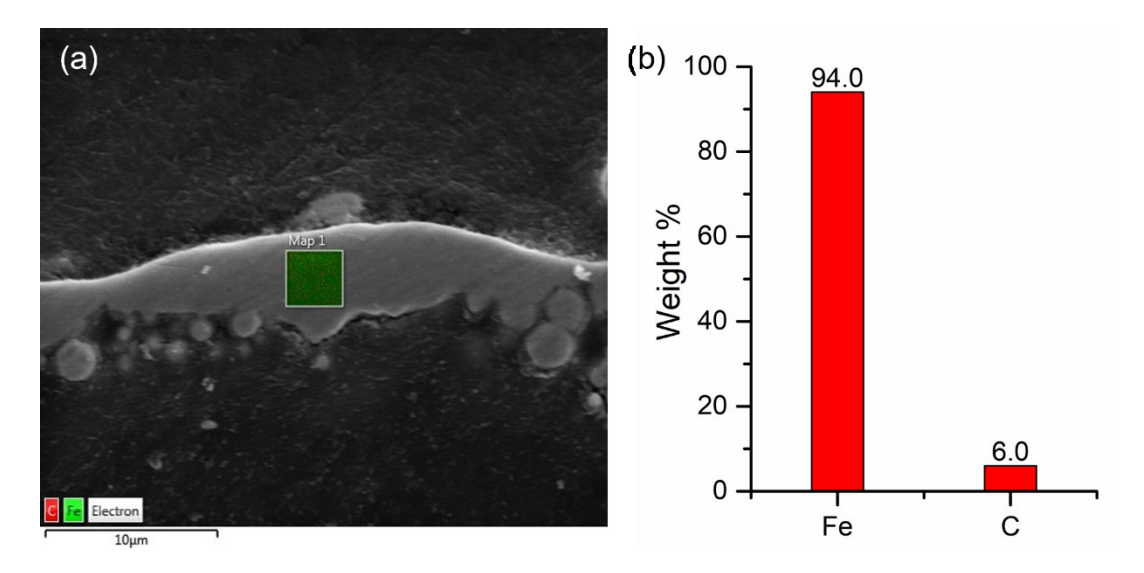
It can be seen from Fig.6a, b and Fig. 7a, b that the cross-sectional images of the samples sintered with DP-LMS show reasonably continuous and densified top thin layers (in the XZ cross section, voids may be seen around inter-track boundaries, which is also implied by the top surface SEM images in Fig.3a and b, showing some pores mainly located around inter-track boundaries).

On the other hand, Figure 6c, d and 7c, d show that the cross sections of the samples sintered with SP-LMS do not show very continuous top thin layers, which consist of multiple

sections that appear to have poor connections with each other. Each section appears to be formed due to melting, coalition, and solidification of powder particles. However, the multiple sections are not well connected with each other. The frequent gaps between adjacent sections imply a high porosity of each layer sintered with SP-LMS. It should be noted that a layer of particles is attached to the bottom of the sintered layer in each SEM image for the SP-LMS samples. This is because the SP-LMS samples are very fragile and can only endure ultrasonic cleaning for just a few seconds and would often be broken by longer ultrasonic cleaning. Thus, typically the SP-LMS samples were ultrasonically cleaned only for a very short duration. Hence, a much larger amount of particles below the sintered layer shows up in the SP-LMS sample images than those in the DP-LMS sample images in Figs. 6 and 7. This also implies a much poorer mechanical strength of the layer sintered with SP-LMS than the layer sintered with DP-LMS.

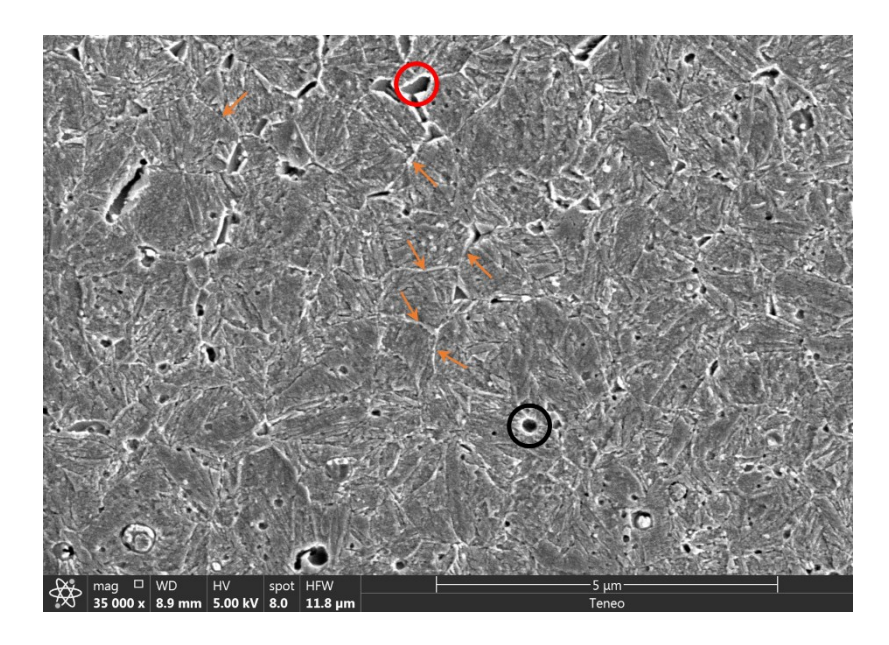
## 3.2 Grain Microstructure, Phase and Nanohardness of Material Sintered by DP-LMS

Figure 8a gives the elemental distribution map measured with EDS for a region in the XZ cross section of a sample sintered with DP-LMS. Figure 8b gives the elemental weight percentages obtained via EDS for the measured region. No detectable oxygen element is shown, implying that argon has prevented obvious iron oxidation during the sintering. The measurement result in Fig.8b shows 6.0% carbon, which is larger than the carbon percentage in the original iron powder given in the product Certificate of Analysis [25] (see Table 1). As introduced earlier, the laser-sintered sample was mounted in epoxy, ground and polished prior to the EDS measurement, and the sample surface could be easily attached with carbon coming from external sources after sintering, which is expected to be the major reason for the 6.0% carbon in the EDS measurement result. As pointed out in Ref. [28], it is challenging to reliably measure the carbon element percentage originally in a sample by EDS due to the wide presence of carbon in the environment.



**Figure 8.** (a) A map showing elemental distributions obtained from an EDS measurement for a cross-sectional region approximately in the XZ plane for an iron layer sample sintered with DP-LMS; (b) the elemental weight percentages obtained via the EDS measurement for the map region in (a) (the EDS result shows no detectable oxygen, indicating the argon environment during DP-LMS is effective in the protection against oxidation).

Figure 9 presents the SEM image for a region of a chemically etched oblique cross section of a sample sintered with DP-LMS, which shows the grain microstructure (the orientation of the cross section has a small angle relative to the sample top surface orientation). In the image, typically the small dents with sharp corners (e.g., the one indicated by the red circle) result from chemical etching, and they are not pores resulting from the sintering process (i.e., they do not exist prior to chemical etching). The approximately circular dents (e.g., the one indicated by the black circle) are typically pores resulting from the sintering process. The chemical etching process has reasonably revealed the grain boundaries, based on which the grain sizes in the image can be very approximately estimated to be typically in the range of ~1 to ~3 μm using the scale bar of the image. In the image, the grains appear roughly equiaxed.



**Figure 9.** An SEM image of a chemically etched region in an oblique cross section of a sample sintered with DP-LMS, showing the grain microstructure (The red circle indicates a dent caused by chemical etching, while the black circle indicates a pore that already exists prior to etching. The orange arrows indicate some of the parent austenite grain boundaries).

The surface and cross-sectional morphologies shown in Figs. 3, 6 and 7 for the samples sintered with DP-LMS suggest that likely full melting of particles have occurred during DP-LMS. Hence, the re-solidification process of the molten material should significantly affect the final grain size. One important reason for the small grain size shown in Fig. 9 is expected to be the high cooling rate [29-31] in re-solidification during DP-LMS. In the authors' previous paper on DP-LMS [17], time-resolved measurements were performed for the cobalt powder bed surface temperature in an approximately elliptical spot of ~50 × ~70 µm surrounding the laser beam center during DP-LMS (called "the small spot surrounding the laser center" next). During the measurement in [17], the small measurement spot and the laser spot stay stationary while the cobalt material is moving at a nominal speed of 20 mm/s. Solid bulk cobalt has a regular density, specific heat and thermal conductivity reasonably similar to those for solid iron [32-34]. Besides, the particle size (nominal size: ~1.6 µm), powder pre-sintering relative density and laser parameters

in Ref. [17] are at least on the same order of magnitude as those in this paper. Thus, the temperature history measured in Ref. [17] can be used to roughly estimate the material cooling rate (at least the order of magnitude) of the DP-LMS process reported in the current paper. Based on the measured temperature history in [17], the material cooling rate at the powder bed surface (for the small spot surrounding the laser center) is roughly estimated to be on the order of magnitude of  $\sim 0.5$  to  $\sim 1 \times 10^6$  K/s when the temperature is near the melting point. The estimation process is very rough, but is expected to approximately reflect at least the order of magnitude of the actual cooling rate, sufficient for the purpose of the discussion below.

Fitting relations between the grain size and the cooling rate have been reported in the literature for different metallic materials. For example, in Ref. [29], the solidification of Ni45 alloy with different high cooling rates has been studied, and the following fitting relation is obtained for the cooling rate range of ~2000 to ~22000 K/s:

$$d = 79 \times \dot{T}^{-0.3} \tag{1}$$

where d denotes the grain diameter ( $\mu$ m) and  $\dot{T}$  represents the cooling rate (K/s). Based on Eq.(1) and the cooling rate of  $\sim 0.5-1\times 10^6$  K/s previously estimated for the DP-LMS process in this paper, a grain size of approximately  $\sim 1.3-1.5$   $\mu$ m is obtained, which is reasonably close to the typical grain size estimated from Fig.9. Ref.[30] shows the following relation between the grain diameter D (in the unit of meter) and the cooling rate near the solidification point for 316 stainless steel within the range of  $\sim 5\times 10^4$  to  $\sim 5\times 10^5$  K/s:

$$D = 1 \times \dot{T}^{-1} \tag{2}$$

Using Eq.(2) and the cooling rate of  $\sim 0.5 - 1 \times 10^6$  K/s, a grain diameter of  $\sim 1 - 2$  µm is obtained, which is still reasonably close to the grain size estimated from Fig. 9. Thus, the grain sizes estimated from both Eqs. (1) and (2) are reasonably close to the grain size in this work estimated

from Fig. 9. Although Eqs. (1) and (2) are fitting relations for metals and cooling rate ranges different from those in this study, such consistency does provide supporting evidence that one important reason for the fine grains shown in Fig. 9 should be the high cooling rate in resolidification during the DP-LMS process. It should also be noted that Ref. [31] studied rapid solidification of pure iron via the piston quenching method, and when the cooling rate at the solidification point is  $\sim 4 \times 10^6$  K/s, the obtained grain sizes are in the range of around 2.6 to 6  $\mu$ m, not very far away from the grain size estimated in this work from Fig. 9.

Figure 10 shows the nanohardness measurement results. Nanoindentation measurements were conducted on the XZ cross section of two samples produced by DP-LMS with six locations measured per sample, leading to twelve measurements in total for the two samples. Figure 10a shows the load-displacement curves for three of the six measurements for Sample 1. Figure 10b shows the hardness values from the six measurements on each sample as well as the average hardness value obtained for each sample. The average hardness measured for both samples is close to ~7.0 GPa. The error bar shown in Fig.10b is the standard deviation for the six measurements.

In this study, for the nanoindentation test on a sample, multiple locations on the XZ cross section of the sintered material were measured. It was intended to make indentation locations close to the central region of the sintered layer in its depth direction; but some actual indentation location(s) could have deviations. If the dent left by an indentation measurement was found to be too close to the edge of the sintered material (i.e., too close to the interface between the sintered material and the mounting epoxy), that particular indentation result was discarded (and the location was not counted in the aforementioned six locations) because it could be obviously affected by the edge effect. Eventually, only the measurement results for indentation locations close to the central region of the sintered layer were kept.

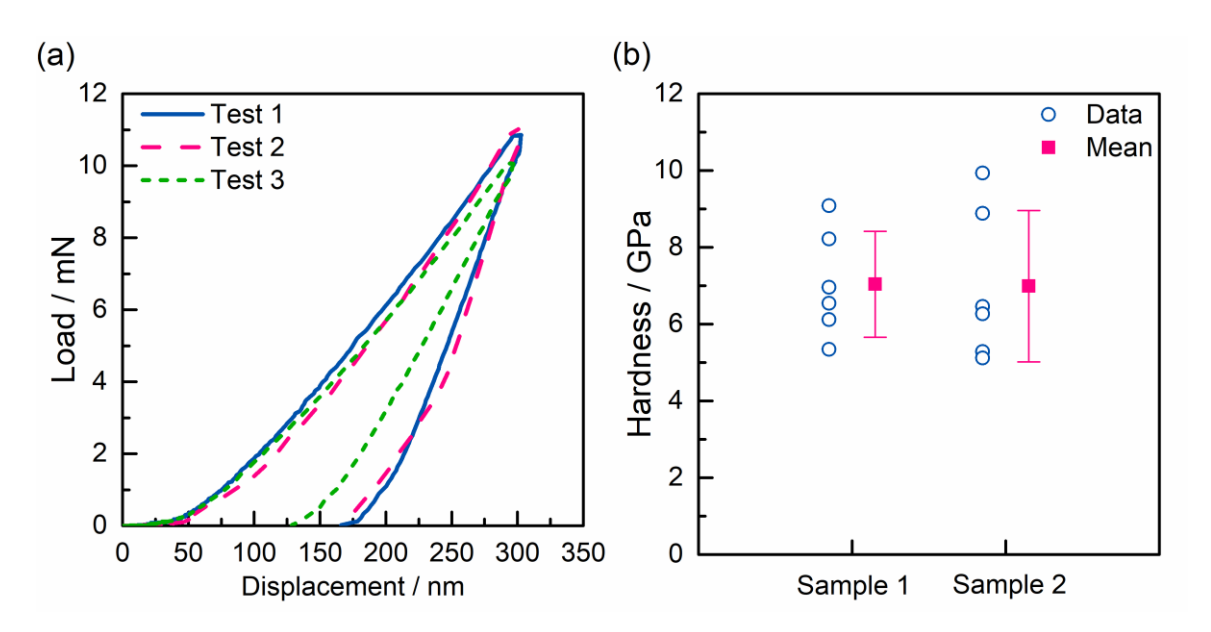


**Figure 10.** Nanoindentation results for samples sintered with DP-LMS: (a) the load-displacement curves from three of the six measurements for Sample 1; (b) Individual measurement and average hardness values for Sample 1 and 2 (each individual hardness value given is the average hardness in the tip penetration depth range of 100 to 200 nm)

Figure 11 shows the measured XRD results. Figure 11a gives the results in a relatively wide-angle range for an original iron powder sample and a sample sintered with DP-LMS, while Figure 11b and c show refined measurement results in a relatively narrow angle range for a powder sample and a sample sintered with DP-LMS, respectively. In the XRD measurements, each DP-LMS "sample" placed in the sample holder contains multiple pieces of the layer sintered by DP-LMS, such that a relatively large top surface area of the sintered material is irradiated by the X-ray spot. The locations of the four major diffraction peaks in Fig.11a (for both the powder and the sintered samples) are reasonably consistent with the locations of the four peaks for the  $\alpha$ -Fe phase [35-37] in the angle range shown in Fig.11a. Hence, the  $\alpha$ -Fe phase should exist in both the original powder and the sintered samples. It is very likely the martensite phase also exists in the sintered sample, which is supported by multiple pieces of evidence. Evidence (1): the original powder contains ~0.66 wt.% carbon according to Ref. [25] as shown in Table 1. The DP-LMS process, as discussed earlier, has likely resulted in full melting of some powder particles, followed by rapid

cooling at a very high rate of  $\sim 0.5-1\times 10^6$  K/s in solidification as roughly estimated earlier. Based on the time-temperature-transformation diagram shown in [38] for 0.65% carbon steel, it is expected that such a high cooling rate is sufficient to form martensite. Evidence (2): the existence of martensite is further supported by the material morphology in the SEM image in Fig.9, where the lath-like microstructures appear reasonably similar to those for steel martensite in SEM images in Refs. [39, 40]. Such laths broadly exist in the entire imaged domain in Fig.9, which indicates that martensite likely exists in the material. Evidence (3): the existence of martensite is also consistent with the high nanohardness shown in Fig.10.

The top X-ray diffraction peak (i.e., the peak with the highest relative intensity) for martensite can be closely located on the left side of the top diffraction peak for  $\alpha$ -Fe [35-37]. Fig.11c shows that for the sintered sample, the profile of the top XRD peak for  $\alpha$ -Fe is significantly asymmetric, and the asymmetricity looks more severe than that for the powder sample shown in Fig.11b. Although other factors such as dislocations and concentration gradients may also contribute to the asymmetricity of an XRD peak [41, 42], the existence of the martensite top peak slightly to the left of the  $\alpha$ -Fe top peak is likely for Fig.11c, considering the multiple pieces of evidence supporting martensite existence as discussed in the previous paragraph.

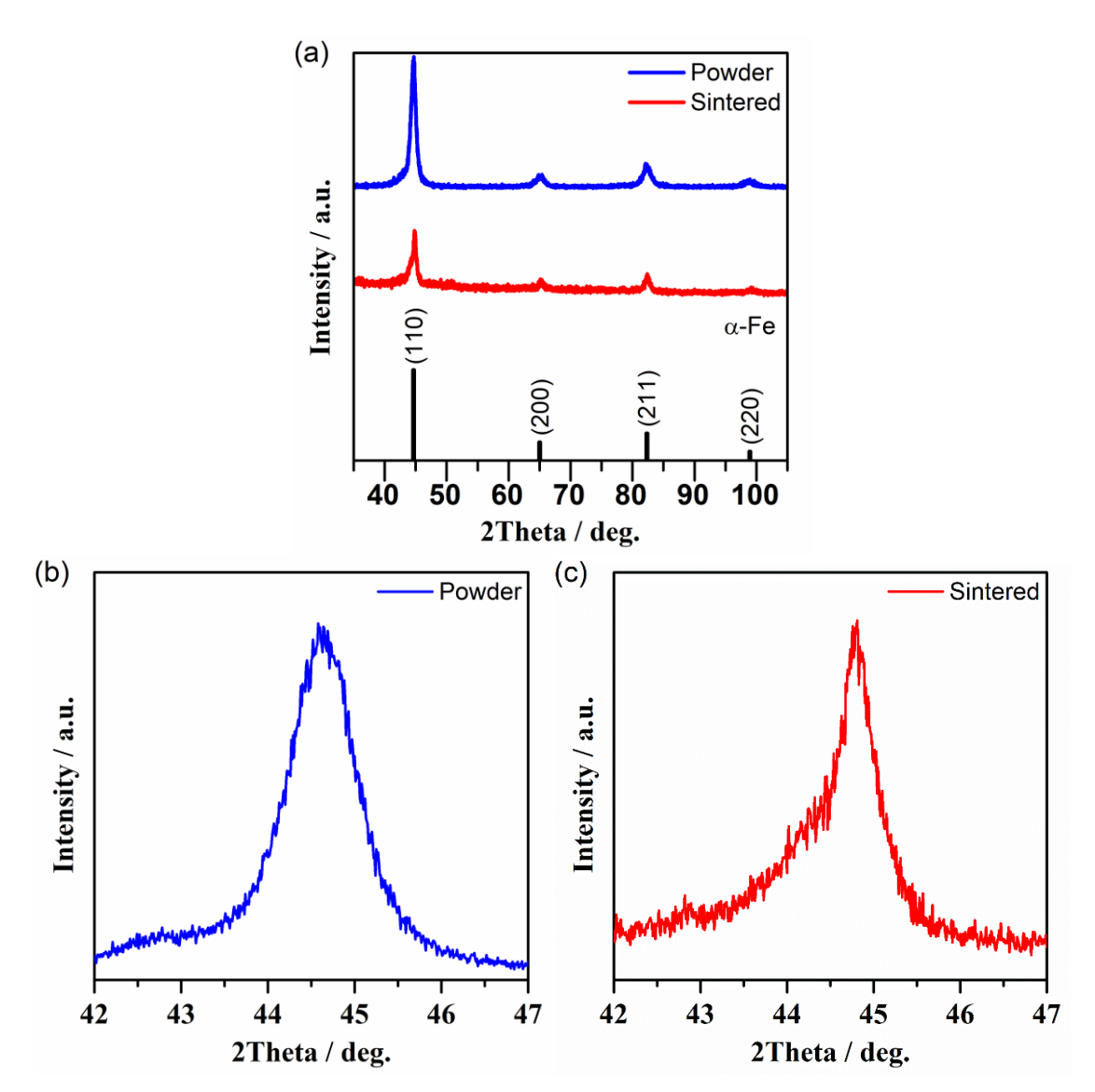


**Figure 11.** XRD measurement results for original iron powder samples and samples sintered with DP-LMS: (a) measurement results in a relatively wide angle range for a powder sample and a sintered sample; (b) and (c) results from refined measurements in a narrow angle range for a powder sample and a sintered sample, respectively.

Ref. [43] reported effective nanohardness of around 2.3 to 3.0 GPa for material made by selective laser melting (SLM) of high-purity iron powders with an original average particle size of ~27 µm (the related SLM process using a CW laser was introduced in Ref.[24]). The measured nanohardness of the material sintered with DP-LMS in this paper is ~7.0 GPa, much larger than the material nanohardness reported in Ref. [43]. This is expected to be related to one or both of the

following factors: (1) the sintered material in this paper likely contains martensite as discussed earlier while the material in Ref. [43] is obtained by SLM of high-purity iron powders with a very low carbon content of only 0.004% and the material after SLM only contains the bcc phase [24]; and (2) the grain size of material sintered in this paper as shown in Fig.9 is estimated to be typically  $\sim$ 1 to  $\sim$ 3  $\mu$ m, much smaller than that for the material in Ref. [43] (which is around  $\sim$ 10  $\mu$ m on average). A small grain size can lead to the Hall-Petch strengthening mechanism, which can be shown in the following equation relating the ferrite grain size (*d*) with the polycrystalline ferrite microstructure yield strength,  $\sigma_y$  [44]:

$$\sigma_{v} = \sigma_{1} + \sigma_{S} + \sigma_{d} + kd^{-0.5} \tag{3}$$

where  $\sigma_1$  is the single crystal iron friction stress,  $\sigma_s$  and  $\sigma_d$  represent the friction stress increase due to solid solution strengthening and dislocations, respectively, and k denotes the Hall-Petch coefficient. Eq.(3) suggests that a smaller grain size will result in a higher yield strength, which may also be correlated with a larger hardness [45].

Ref. [46] reports that the intrinsic martensite nanohardness for a low-carbon steel with a 0.2 wt.% carbon content is  $\sim$ 6.25 GPa. Ref. [47] shows that the Fe-C martensite nanohardness is  $\sim$ 10 GPa for a 0.6 wt.% carbon content. The material sintered with DP-LMS in this paper likely contains both martensite and  $\alpha$ -Fe phases, and thus its measured nanohardness of  $\sim$ 7.0 GPa is a reasonable value compared with those reported in [46, 47] for martensite and that in [43] for a fully bcc iron phase (which is  $\sim$ 2.3 to 3 GPa).

#### 3.3 Strategic Guidelines for Parameter Selection in DP-LMS

Finally, some strategic guidelines on the parameter selection in DP-LMS will be discussed. As already introduced in Ref. [17], typically the selection of parameters in DP-LMS should follow the following strategic guidelines:

**Guideline 1:** The pressing pulse intensity needs to be large enough to generate sufficiently high pressures onto the surface of the powder bed. For a given laser spot size, this guideline typically implies the selection of a relatively short pulse duration and a sufficiently large pulse energy for the pressing laser pulse.

**Guideline 2:** It is often desirable that the material surface area irradiated by the pressing pulse is still in a molten or partially molten state right before the pressing pulse arrives. Typically, this guideline implies that the pressing pulse delay time  $\tau_p$  should be sufficiently small.

If Guidelines 1 and 2 are followed, then potentially the pressing laser pulse can induce high pressures onto the surface of molten powder material to promote their flow to fill voids, reduce balling, and/or improve material continuity.

In addition to the aforementioned two guidelines already discussed in the authors' previous paper [17], an additional guideline is introduced below in this paper:

Guideline 3: It is often desirable that the melt pool lifetime induced by each laser pulse group is short enough to avoid excessive melt flow driven by surface tension after the end of the pressing laser pulse. Different from the melt flow driven by the pressing laser pulse, the flow driven by surface tension may often hurt the continuity and/or densification of the material solidified from the melt pool (as discussed in detail below). Typically, this guideline implies the total incoming energy from each laser pulse group should not be too large and adjacent pulse groups should be sufficiently separated in time. The melt pool lifetime here mainly refers to the melt pool duration during which the pool size is large enough to permit obvious melt flow driven by surface tension.

The likely fundamental mechanism for Guideline 3 will be discussed next. In DP-LMS, typically in each pulse group it is desirable that the pressing pulse follows the last previous sintering pulse sufficiently close in time such that the material surface region irradiated by the pressing laser pulse is still melted or partially melted right before the pressing pulse arrives [17]. The high pressures generated by the pressing laser pulse can promote melt flow to fill voids, reduce balling, and/or improve material continuity. The melt pool may still exist for a certain period after the pressing laser pulse is over. During this period, surface tension may drive further material flow in the melt pool [48-50]. Different from the flow driven by the pressing pulse, the flow driven by surface tension, if lasts sufficiently long, could often hurt the continuity and/or densification of material solidified from the melt pool. For example, the thermocapillary flow driven by a surface tension gradient (Marangoni effect) might occur, and could potentially cause a larger amount of molten material moving out of a certain portion of the melt pool than the amount of material moving in [48, 50]. This could cause depression in that portion of the melt pool [48], leading to poor continuity or even segmentation in the material solidified from the melt pool. Thus, it is often desirable to avoid an overlong melt pool lifetime to prevent excessive melt flow driven by surface tension after the end of the pressing laser pulse.

The comparison of the single-track sintering results in Fig.12a and b is a likely demonstration of the harmful effect of excessive melt flow driven by surface tension after the end of the pressing laser pulse due to an overlong melt pool lifetime in DP-LMS. Figure 12a shows a single track on an iron powder bed surface sintered with DP-LMS using the same laser parameters as those for the results in Fig. 3 ( $E_1$ : ~0.048 mJ,  $E_2$ : ~0.124 mJ,  $E_3$ : ~150 µm and  $E_3$ : ~110 µm). Each laser pulse group comprises 10 sintering pulses as well as 1 pressing pulse as shown in Fig. 1b. For Fig.12a, the incoming energy from each laser pulse group is around 0.604 mJ. Figure 12b

shows a single track sintered with DP-LMS using laser parameters the same as those for Fig.12a, except a larger sintering pulse energy of  $E_1 = \sim 0.080$  mJ. For Fig.12b, the laser energy input from each laser pulse group is around 0.924 mJ, about 53.0% higher than that for Fig. 12a. As a result, compared with Fig.12a, each laser pulse group for Fig.12b is expected to produce a longer melt pool lifetime in the powder bed. The sintered track in Fig. 12b appears more segmented and less continuous than that in Fig.12a. The material irregularity and segmentation in the sintered track in Fig.12b is expected to be due to the excessive melt flow driven by surface tension after the end of the pressing laser pulse due to an overlong melt pool lifetime.

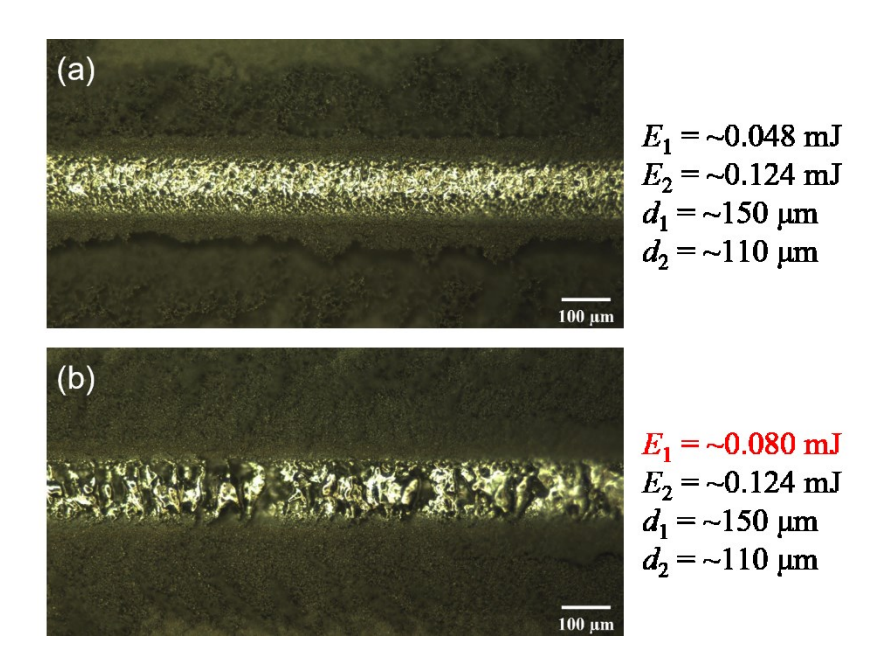


**Figure 12.** Single-track sintering results with DP-LMS using  $E_1$ =~0.048 mJ (a) and ~0.080 mJ (b), respectively ( $E_1$ : sintering pulse energy,  $E_2$ : pressing pulse energy,  $e_1$ : sintering laser spot diameter,  $e_2$ : pressing laser spot diameter).

As introduced earlier, DP-LMS can produce a much lower surface porosity than SP-LMS as shown in Fig.5. Meanwhile, some pores still exist (particularly around the inter-track boundaries) in the DP-LMS results in Fig.3a and b. This is likely related to the fact that the very fine iron powder used has a high pre-sintering porosity of ~50%. It could be good work in the future to further improve the sintering quality and reduce the porosity, possibly via a systematic

optimization of multiple laser parameters involved (not just the optimization of one parameter) and/or pre-heating of the powder during DP-LMS.

#### 4. Conclusions

This paper reported experimental studies on a novel patented DP-LMS process previously put forward by the corresponding author [21]. In each sintering process, a thin layer was sintered via DP-LMS with a laser spot scanning multiple overlapping tracks on the surface of an iron powder bed with small particle sizes. The top surface and cross sections of the samples sintered were observed using SEM. The top surface porosity (i.e., the pore area percentage) was estimated based on SEM images using ImageJ. EDS and XRD measurements were conducted on the material sintered. The material grain microstructure was observed via SEM after chemical etching. The sintered material nanohardness was measured via nanoindentation. Under the conditions studied, the following has been found:

- (1) The top surface porosity of the iron layer sintered with DP-LMS is ~3.4%, much lower than that by SP-LMS (i.e., laser micro sintering utilizing only the "sintering laser pulses", but not the "pressing laser pulses"), where the porosity is ~19.0%. The cross sections of the iron layer sintered with DP-LMS look much more densified and continuous than those with SP-LMS.
- (2) The SEM image of the DP-LMS sample cross section in Fig. 9 shows roughly equiaxed grains with a typical grain size of  $\sim$ 1 to  $\sim$ 3  $\mu$ m. One important reason for the small grain size is expected to be the high cooling rate of the material in re-solidification during DP-LMS, estimated to be on the order of magnitude of  $\sim$ 0.5 1 × 10<sup>6</sup> K/s based on the authors' previous related work.
- (3) The nanoindentation measurements performed show that the material sintered with DP-LMS has a high nanohardness of ~7.0 GPa, which is likely due to the small grain size and/or the

existence of martensite phase.

(4) To obtain good sintering results in DP-LMS, the sintering pulse energy should not be too large. Otherwise, the sintered material may show poor continuity. This is likely because the overlarge sintering pulse energy can lead to an overlong melt pool lifetime for each laser pulse group, during which the melt flow driven by surface tension could cause irregularity and even segmentation in the material solidified from the melt pool.

Some good potential future work may include (but not necessarily limited to): (1) the further improvement of the process parameters to further enhance the sintering quality by DP-LMS; (2) the production of metal parts with complicated geometries by DP-LMS; and (3) the study of the potential application of DP-LMS for ceramic materials.

## **Declaration of Competing Interest**

This paper's corresponding author, Prof. Benxin Wu, is also the inventor for the granted patent on double-pulse laser micro sintering described in [21].

#### Acknowledgment

This material is based upon work supported by the National Science Foundation under Grant No. CMMI 1728481. The grantee institute of this NSF award is Purdue University (West Lafayette, Indiana, USA). This paper's corresponding author, Prof. Benxin Wu, is also the inventor for the granted patent on double-pulse laser micro sintering described in [21]. The authors would like to thank Prof. Kejie Zhao and Mr. Xiaokang Wang at Purdue University, who performed the nanoindentation measurements and provided the measurement results and measurement-related information reported in this paper. The authors would like to thank Dr. Xingtao Liu for the valuable discussion on microstructure characterization, together with Dr. Jung-ting Tsai and Dr. Sae Matsunaga for the help in sample preparation and chemical etching. The authors also would like to greatly thank Prof. David F. Bahr at Purdue, as well as Dr. Yailuth Alexandra Loaiza Lopera, Shiang Jiun Horng, Cheng-Hsiu Shih, and Chase Wikberg for their relevant help.

#### **List of References**

- 1. J.P. Kruth, P. Mercelis, J. Van Vaerenbergh, L. Froyen, M. Rombouts, Binding mechanisms in selective laser sintering and selective laser melting, Rapid Prototyping Journal. 11 (2005) 26-36.
- 2. Y. Wang, J. Shi, S. Lu, Y. Wang, Selective laser melting of graphene-reinforced Inconel 718 superalloy: evaluation of microstructure and tensile performance, Journal of Manufacturing Science and Engineering. 139 (2017) 041005.
- 3. N. Guo, M.C. Leu, Additive manufacturing: technology, applications and research needs, Frontiers of Mechanical Engineering. 8 (2013) 215–243.
- 4. X. Zhang, C.J. Yocom, B. Mao, Y. Liao, Microstructure evolution during selective laser melting of metallic materials: A review, Journal of Laser Applications. 31(2019) 031201.
- 5. J. Huang, M. Li, J. Wang, Z. Pei, P. McIntyre, C. Ma, Selective laser melting of tungsten: Effects of hatch distance and point distance on pore formation, Journal of Manufacturing Processes. 61 (2021) 296-302.
- 6. P. Fischer, M. Locher, V. Romano, H.P. Weber, S. Kolossov, R. Glardon, Temperature measurements during selective laser sintering of titanium powder, International Journal of Machine Tools and Manufacture. 44(12) (2004) 1293-1296.
- 7. L. Caprio, A.G. Demir, B. Previtali, Influence of pulsed and continuous wave emission on melting efficiency in selective laser melting, Journal of Materials Processing Technology. 266 (2019) 429-441.
- 8. L. Caprio, A.G. Demir, B. Previtali, Comparative study between CW and PW emissions in selective laser melting, Journal of Laser Applications. 30(3) (2018) 032305.
- 9. H. Song, Z. Kang, B. Wu, Nanosecond pulsed laser sintering of carbon nanotube–Silver nanocomposite thin films on a flexible substrate: In-situ temperature measurements and post-process characterizations, Journal of Manufacturing Processes. 79 (2022) 476-85.
- 10. H. Song, M. Wu, W. Liu, B. Wu, Thermal modeling and validation via time-resolved temperature measurements for nanosecond laser irradiation of a powder bed of micro metal particles, Optics & Laser Technology. 152 (2022) 107981.
- 11. P. Regenfuss, A. Streek, L. Hartwig, S. Klötzer, Th. Brabant, M. Horn, R. Ebert, H. Exner, Principles of laser micro sintering, Rapid Prototyping Journal. 13 (2007) 204-212.
- 12. A. Streek, P. Regenfuss, H. Exner, Fundamentals of energy conversion and dissipation in powder layers during laser micro sintering, Physics Procedia. 41 (2013) 851–862.
- 13. H. Zhu, L. Ke, W. Lei, C. Dai, B. Chen, Effect of the Q-switch parameters on the sintering behavior of laser micro sintering Cu-based metal powder using Q-switched Nd-YAG laser, Rapid Prototyping Journal. 19 (2013) 44-50.
- 14. L. Ke, H. Zhu, J. Yin, X. Wang, Effects of peak laser power on laser micro sintering of nickel powder by pulsed Nd: YAG laser, Rapid Prototyping Journal. 20 (2014) 328-335.
- 15. A. Streek, P. Regenfuss, R. Ebert, H. Exner, "Laser micro sintering—a quality leap through improvement of powder packing", 2008 International Solid Freeform Fabrication Symposium.
- 16. M. Vaezi, H. Seitz, S. Yang, A review on 3D micro-additive manufacturing technologies, The International Journal of Advanced Manufacturing Technology. 67 (2013) 1721-1754.

- 17. W. Liu, H. Song, B. Wu, H. You, Double-pulse laser micro sintering: Experimental study and mechanism analysis aided by in-situ time-resolved temperature measurements, Journal of Manufacturing Processes. 69 (2021) 191-203.
- 18. U. Ali, Y. Mahmoodkhani, SI. Shahabad, R. Esmaeilizadeh, F. Liravi, E. Sheydaeian, K.Y. Huang, E. Marzbanrad, M. Vlasea, E. Toyserkani, On the measurement of relative powder-bed compaction density in powder-bed additive manufacturing processes, Materials & Design. 155 (2018) 495-501.
- 19. G. Jacob, C.U. Brown, A. Donmez, The influence of spreading metal powders with different particle size distributions on the powder bed density in laser-based powder bed fusion processes, Gaithersburg, MD: US Department of Commerce, National Institute of Standards and Technology, 2018.
- 20. S.E., Brika, M. Letenneur, C.A. Dion, V. Brailovski, Influence of particle morphology and size distribution on the powder flowability and laser powder bed fusion manufacturability of Ti-6Al-4V alloy, Additive Manufacturing. 31 (2020) 100929.
- 21. B. Wu, inventor; Purdue Research Foundation, assignee. Processes and systems for double-pulse laser micro sintering. United States patent. Patent No.: US11,440,099 B2. Date of Patent: 09/13/2022 (related provisional patent application number: 62693684, filed on 07/03/2018).
- 22. H. Song, Z. Kang, Z. Liu, B. Wu, Experimental study of double-pulse laser micro sintering: A novel laser micro sintering process, Manufacturing Letters. 19 (2019) 10-4.
- 23. C.A. Schneider, W.S. Rasband, K.W. Eliceiri, NIH Image to ImageJ: 25 years of image analysis, Nature methods. 9(7) (2012) 671-675.
- 24. P. Lejček, M. Roudnická, J. Čapek, D. Dvorský, J. Drahokoupil, D. Šimek, J. Čížek, P. Svora, O. Molnárová, D. Vojtěch, Selective laser melting of pure iron: multiscale characterization of hierarchical microstructure, Materials Characterization. 154 (2019) 222-32.
- 25. Alfa Aesar, Certificate of Analysis, Product No.: 40337, Product: Iron powder, spherical, 1-3 micron, 98+%.
- 26. X. Li, B. Bhushan. A review of nanoindentation continuous stiffness measurement technique and its applications, Materials characterization. 48 (2002) 11-36.
- 27. Y.F. Shen, D.D. Gu, Y.F. Pan, Balling process in selective laser sintering 316 stainless steel powder, Key Engineering Materials. 315 (2006) 357-360.
- 28. SEM Elemental Analysis (EDS, EDX), http://www9.open.ac.uk/emsuite/services/sem-eds-0 (last accessed on November 8, 2022).
- 29. J. Shao, G. Yu, X. He, S. Li, R. Chen, Y. Zhao, Grain size evolution under different cooling rate in laser additive manufacturing of superalloy, Optics & Laser Technology. 119 (2019) 105662.
- 30. B. Cantor, Fundamentals of rapid solidification, in: P.R. Sahm, H. Jones, C.M. Adam eds., Science and technology of the undercooled melt: rapid solidification materials and technologies. Martinus Nijhoff Publishers, 1986.
- 31. F. Duflos, B. Cantor, Cooling rate measurements on pure iron rapidly solidified by piston quenching, Journal of materials science. 22 (1987) 3765-3770.
- 32. The Iron Triad: Iron, Cobalt, and Nickel. (Last updated: August 25, 2020). Last accessed on November 4 2022, from https://chem.libretexts.org/@go/page/24345

- 33. Thermal Properties of Metals, Conductivity, Thermal Expansion, Specific Heat. https://www.engineersedge.com/properties\_of\_metals.htm (last accessed on November 4, 2022).
- 34. A.H. Fleitman, R.B. Herchenroeder, J.G.Y. Chow, Cobalt-base alloys for use in nuclear reactors, Nuclear Engineering and Design. 15 (1971) 345-62.
- 35. S. Gates-Rector, T.N. Blanton, The Powder Diffraction File: a quality materials characterization database, Powder Diffr. 34 (2019) 352-60.
- 36. PDF-4+ 2022 (version 4.2201) and PDF4/Organics 2022 (version 4.2221), edited by Dr. Soorya Kabekkodu, International Centre for Diffraction Data, Newtown Square, PA, USA.
- 37. H.E. Swanson, R.K. Fuyat, and G.M. Ugrinic, Standard X-ray Diffraction Powder Patterns, National Bureau of Standards (U. S.), Circular 539 (1955) IV: 3-5.
- 38. A. Kartono, N. Tofany, M.F. Ahmad, M. Mamat, M.L. Husain, Applications of Crank-Nicolson method with ADI in laser transformation hardening, Heat and Mass Transfer. 48 (2012) 2041-57.
- 39. M.X. Wei, S.Q. Wang, X.H. Cui, K.M. Chen, Characteristics of extrusive wear and transition of wear mechanisms in elevated-temperature wear of a carbon steel, Tribology Transactions. 53 (2010) 888-96.
- 40. Q. Wang, Q. Ye, Y. Tian, T. Fu, Z. Wang, Superior through-thickness homogeneity of microstructure and mechanical properties of ultraheavy steel plate by advanced casting and quenching technologies, Steel Research International. 92 (2021) 2000698.
- 41. S. Takebayashi, T. Kunieda, N. Yoshinaga, K. Ushioda, S. Ogata, Comparison of the dislocation density in martensitic steels evaluated by some X-ray diffraction methods, ISIJ International. 50(6) (2010) 875-82.
- 42. T. Ungár, Dislocation densities, arrangements and character from X-ray diffraction experiments, Materials Science and Engineering: A. 309-310 (2001) 14-22.
- 43. P. Lejček, J. Čapek, M. Roudnická, O. Molnárová, J. Maňák, J. Duchoň, D. Dvorský, M. Koller, H. Seiner, P. Svora, D. Vojtěch, Selective laser melting of iron: Multiscale characterization of mechanical properties, Materials Science and Engineering: A. 800 (2021) 140316.
- 44. F. Duflos, R. Cantor, Overview 15 The microstructure and kinetics of martensite transformations in splat-quenched Fe and Fe-Ni alloys—I. Pure Fe, Acta Metallurgica. 30 (1982) 323-42.
- 45. E.J. Pavlina, C.J. Van Tyne, Correlation of yield strength and tensile strength with hardness for steels, Journal of Materials Engineering and Performance. 17(6) (2008) 888-93.
- 46. B.B. He, M.X. Huang, Revealing the intrinsic nanohardness of lath martensite in low carbon steel, Metallurgical and Materials Transactions A. 46A (2015) 688-94.
- 47. T. Ohmura, K. Tsuzaki, S. Matsuoka, Nanohardness measurement of high-purity Fe–C martensite, Scripta Materialia. 45 (2001) 889-94.
- 48. J. Mazumder, Invited paper an overview of melt dynamics in laser processing, Proc. SPIE 0801, High Power Lasers: Sources, Laser-Material Interactions, High Excitations, and Fast Dynamics, 801 (1987) 228-241.

- 49. I. Yadroitsev, A. Gusarov, I. Yadroitsava, I. Smurov, Single track formation in selective laser melting of metal powders, Journal of Materials Processing Technology. 210 (2010) 1624-1631.
- 50. S.A. Khairallah, A.T. Anderson, A. Rubenchik, W.E. King, Laser powder-bed fusion additive manufacturing: Physics of complex melt flow and formation mechanisms of pores, spatter, and denudation zones, Acta Materialia. 108 (2016) 36-45.

**Table 1**: The original elemental composition of the iron powder used for the laser sintering experiments in this work according to the product Certificate of Analysis from Alfa Aesar [25].

Element	Fe	С	N	О
Weight %	98.18	0.66	0.69	0.47

**Table 2:** The original particle size distribution of the iron powder utilized in the laser sintering experiments in this work, according to the product Certificate of Analysis from Alfa Aesar [25].

Percentage	10%	50%	90%
Particle size (μm)	0.87	1.98	4.24